International Forum on Aeroelasticity and Structural Dynamics
IFASD 2017
25-28 June 2017, Como - Italy

DYNAMIC MANEUVER LOADS CALCULATION FOR A SAILPLANE AND COMPARISON WITH FLIGHT TEST

Arne Voß[1], Gabriel Pinho Chiozzotto[1] and Per Ohme[2]

[1] DLR - German Aerospace Center
Institute of Aeroelasticity
Bunsenstr. 10, 37073 Göttingen, Germany
arne.voss@dlr.de

[2] DLR - German Aerospace Center
Institute of Flight Systems
per.ohme@dlr.de

Keywords: dynamic maneuver loads, flight test, sailplane, preliminary design, aeroelasticity, structural dynamics.

Abstract: This work presents the results of dynamic maneuver simulations of a sailplane and the comparison to flight test data. The goal of the effort is to extend and validate an in-house toolbox used for loads analysis of free-flying flexible aircraft in the time domain. The underlying aerodynamic theories are the steady Vortex Lattice and the Doublet Lattice Method with a rational function approximation (RFA) for the unsteady simulations in the time domain. The structural model comprises a beam model to represent the stiffness properties and a lumped mass model, both are developed using preliminary design methods. Steady aeroelastic trim simulations are performed and used as initial condition for the time simulation of the unsteady maneuvers in which the pilot's commands, which were recorded during flight test, are prescribed at the control surfaces. Two vertical maneuvers with elevator excitation and two rolling maneuvers with aileron excitation are simulated. The validation focuses on the comparison of interesting quantities such as section loads, structural accelerations and the rigid body motion. Good agreement between simulation and flight test data is demonstrated for both vertical and rolling maneuvers, confirming the quality of the models developed by the preliminary design methods.

1 INTRODUCTION

DLR has a large number of activities in aircraft preliminary design [1–7] and in the operation of a fleet of research aircraft [8, 9], requiring in-depth expertise in loads analysis and modeling. The DLR project iLOADS [10] was started with the objective to improve the loads process in the DLR. The expertise in loads analysis is combined and integrated into a comprehensive loads process [11]. Such a process has been formally defined, and global rules for analysis and documentation have been set. Selected numerical methods for loads analysis have been evaluated, and the loads process has been used for investigating the influence of different analysis approaches on aircraft structural design [12]. Finally, the process is subject to verification and validation on different aircraft configurations, numerically as well as experimentally [13]. In this work, the simulation capabilities for dynamic flight maneuvers and resulting structural loads are tested and compared to flight test data from the DLR's Discus-2c sailplane [14]. For the simulation of the dynamic maneuver loads, the in-house software Loads Kernel is selected. The Discus-2c is equipped with over a dozen strain gauges

to measure the structural deformation and loads during flight. A flight test campaign has been prepared [15] and analyzed [16,17] by the DLR Institute of Flight Systems. Because the measurement equipment has been extensively calibrated, the results are expected to be reliable and are used for validation of the simulation. The mass and stiffness models of the Discus-2c used for the numerical simulations are built using simplified approaches from preliminary design methods.

This leads to the following three objectives for this work:

- Asses the applicability of simplified formulations (preliminary design) in the development of models for dynamic maneuver loads analyses
- Test the capabilities of the loads process for the simulation of dynamic maneuver loads in the time domain
- Validate simulation results against flight test data

Aeroelastic models of existing aircraft usually are proprietary of an aircraft company. In addition, only aircraft dedicated to flight testing are equipped with measurement systems. Few institutions operate such aircraft. These are probably the reasons why, to the authors' best knowledge, there are few publications concerning dynamic maneuver loads calculation including a comparison to flight test data. The works by Montel and Thielecke [18] involve empennage loads measurements of the ultra light aircraft UW-9 Sprint for the validation of a loads observer. Eller and Ringertz [19,20] performed flight tests with the ASK21 sailplane and focused on flight mechanical aspects, flutter and aeroservoelastics. Load tests of the Lockheed L-1011 TriStar, developed in the 1970s, were used for tool validation at Lockheed [21–23]. Climent et al. [24] and Claverías et al. [25] present a wake vortex encounter of the A400M and compare numerical simulation to measured loads, demonstrating the capabilities of the tool-sets available at Airbus.

This paper is organized as follows: In Sections 2 and 3 of this work, the set-up of the aeroelastic models (mass, stiffness, aerodynamic and coupling model) is presented. In Sections 4 and 5 the theoretical background of the selected methods is formulated. Section 6 briefly describes the measurement equipment and the procedure of the flight test campaign. The resulting data is compared to the simulation results in Section 7. In the last Section, a conclusion is drawn and an outlook on future work and on possible improvements is given.

2 PRELIMINARY STIFFNESS AND MASS MODELS

The stiffness and mass models for the loads analysis are developed with simple preliminary design methods. It is also an objective of this work to verify the applicability of such

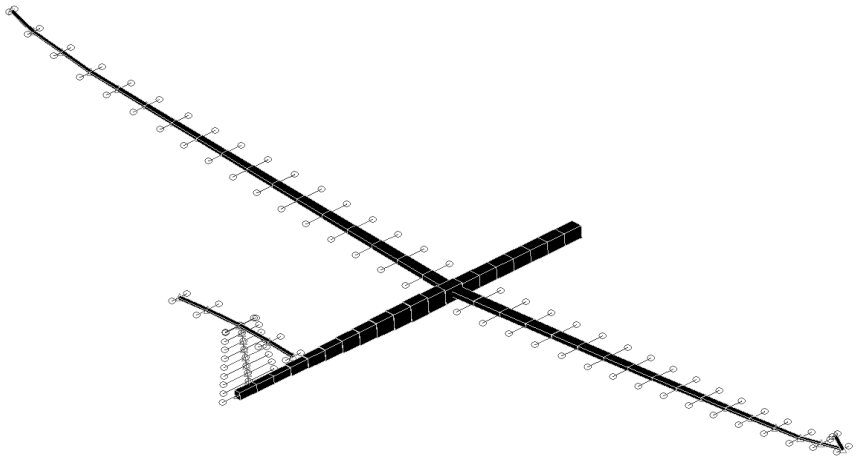

Figure 1: Structural model of the Discus-2c

simplified formulations in the development of loads models for dynamic analyses. The verification with flight test data is in this case an important step in increasing confidence in such quick models for initial analysis.

The stiffness model is based on a beam model. The wing stiffness and mass distribution is estimated with the following process:

1. The wing lift during a pull-up maneuver is calculated and compared to the one of a quasi-static gust. The highest lift force is selected for structural sizing;
2. The wing lift distribution is calculated from the total lift which results from applying a distribution according to Schrenk [26];
3. The wing inertia distribution is proportional to the local chord squared times the airfoil thickness to chord ratio $c^2 \cdot (t/c)$;
4. The wing shear force and bending moment along the span are integrated from the wingtip to the wing root;
5. The spar caps are sized according to the material allowable and the local bending moment. The spar webs are sized according to the material allowable and the local shear force. The torsion cell is sized according to the torsion loads. The final selected thicknesses correspond to the maximum from the sized thickness and minimum gauge requirements.
6. The stiffness properties are calculated analytically at each wing cross-section.

The fuselage stiffness model is estimated from the fuselage geometry and a minimum thickness requirement. The horizontal tailplane (HTP) stiffness is based on the wing stiffness and is scaled to reflect its size. The vertical tailplane (VTP) is assumed rigid. The final beam model is shown in Figure 1. The beam dimensions represent the stiffness properties.

The mass model is obtained by distributing the known masses of each component proportional to areas, volumes or concentrated as point masses. The fuselage mass is distributed proportional to the structural cross-section area. The wing, HTP and VTP masses are distributed proportional to $c^2 \cdot (t/c)$. The center of gravity of the sections along the wing is at 45% of the local chord. A non-dimensional radius of gyration equal to 0.26 relative to the local chord is used to estimate the local pitching moment of inertia. Pilot and equipment masses are placed as concentrated point masses. The final mass model is shown in Figure 2. The spheres visualize the lumped mass distribution. The light, transparent sphere visualizes the total aircraft mass and is located at the center of gravity. Finally, a modal analysis is

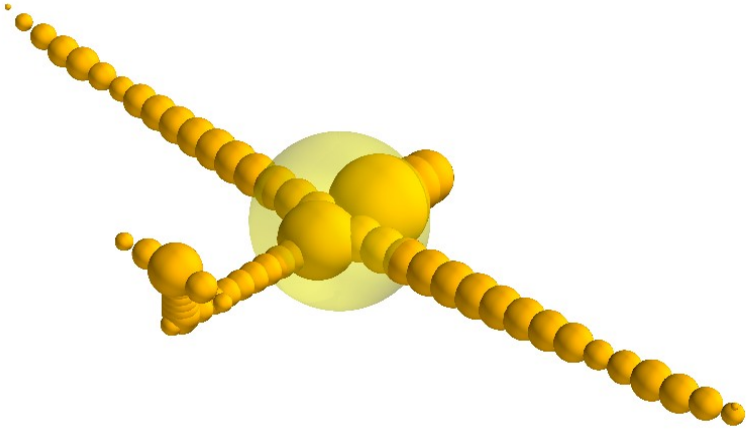

Figure 2: Mass model of the Discus-2c

performed. The mode shapes and corresponding frequencies are compared to data obtained during a ground vibration test and show a satisfactory agreement.

3 AERODYNAMIC MODEL AND AERO-STRUCTURAL COUPLING

The classical aerodynamic approach with the steady Vortex Lattice Method (VLM) and the unsteady Doublet Lattice Method (DLM) is chosen. The formulation of the VLM follows closely the derivation given by Katz & Plotkin [27] using horse shoe vortices. The DLM is formulated as given by Rodden [28,29]. The implementation in Matlab is available from Kotikalpudi [30,31] and was slightly adapted to respect the dihedral of the wings. In addition, the Prandtl-Glauert Transformation with $\beta=\sqrt{(1-Ma^2)}$ is applied to the VLM as suggested by Hedman [32]. The DLM is based on a matrix of aerodynamic influence coefficients (AIC), which depends on the Mach number Ma and reduced frequency k defined in Equation (2). With $k=0$ for the quasi static case, the solution of the DLM is equivalent to the VLM [33]. The AIC matrix relates an induced downwash w_j on each aerodynamic panel to a complex pressure coefficient c_p as stated in Equation (1). The aerodynamic mesh used for the Discus-2c is shown in Figure 3. Camber and twist of the wing is not included.

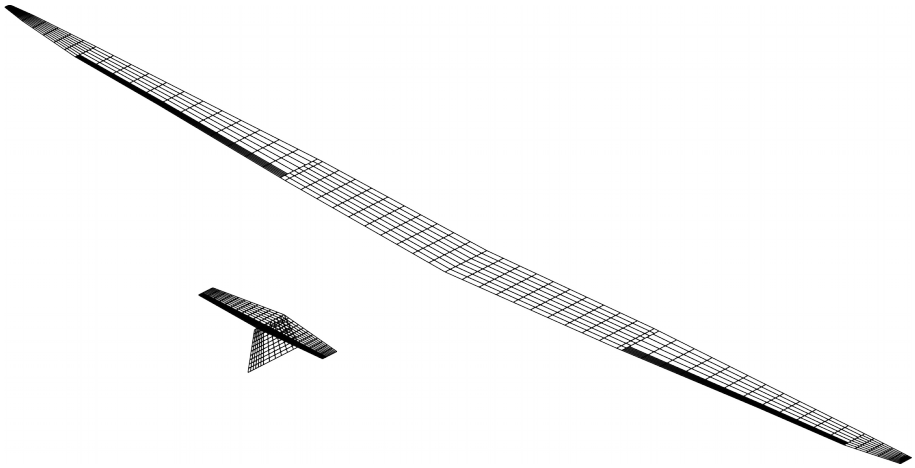

Figure 3: Aerodynamic mesh of the Discus-2c

$$\Delta c_p = AIC(Ma,k)\cdot w_j \tag{1}$$

$$k=\frac{c_{ref}/2}{U_\infty}\cdot\omega \tag{2}$$

$$P_k^{aero,steady}=q_\infty S_{kj} AIC^{steady}\left(D_{jrbm}u_{rbm}+D_{jcs}u_{cs}+D_{jk}^1 T_{kg}\Phi_{gf}u_f+D_{jk}^2 T_{kg}\Phi_{gf}\dot{u}_f\right)\frac{1}{U_\infty} \tag{3}$$

with

q_∞	dynamic pressure
S_{kj}	aerodynamic integration matrix
AIC	AIC-matrix
D_{jrbm}	differential matrix of rigid body motion
D_{jcs}	differential matrix control surface deflections
D_{jk}^1	differential matrix of deformation
D_{jk}^2	differential matrix of velocity
u_{rbm}	rigid body motion
u_{cs}	control surface deflections

u_f flexible structural deformation

$\dot{u}_f$ flexible structural motion

T_{kg} spline matrix for aero-structural coupling

Φ_{gf} modal matrix of flexible structural modes

U_∞ free stream velocity, equal to flight velocity

The calculation of the steady aerodynamic forces is given by Equation (3) (Ref. [34]), containing several sources of aerodynamic forces. Forces by rigid body motions are given by the term $D_{jrbm} u_{rbm}$ and control surface deflections are considered in $D_{jcs} u_{cs}$. Structural flexibility is incorporated in the two terms $D^1_{jk} T_{kg} \Phi_{gf} u_f$ and $D^2_{jk} T_{kg} \Phi_{gf} \dot{u}_f$ for the structural deformation and motion respectively. Using an AIC-matrix approach leads to a local pressure distribution which is integrated and translated to the structural grid using matrices S_{kj} and T_{kg}. As the AIC-matrix is normalized with the dynamic pressure q_∞, the resulting loads need to be multiplied with q_∞ to obtain forces and moments. In this implementation, forces from the different sources given in Equation (3) are calculated independently and superimposed as shown in Equation (4).

$$P_k^{aero,steady} = P_k^{aero,rbm} + P_k^{aero,cs} + P_k^{aero,flex} \tag{4}$$

$$P_k^{aero} = P_k^{aero,steady} + P_k^{aero,unsteady} \tag{5}$$

Unsteady aerodynamic forces in the time domain are obtained by a rational function approximation (RFA) as suggested by Roger [35] and are added to the steady aerodynamic forces in Equation (5). The implementation is base on the work of Gupta [36], Kier and Looye [37] and Karpel and Strul [38]. A difference is the approximation on panel level using physical coordinates. This leads to a large number of lag states but the implementation is more generic and leads to physical, nodal forces. This is desirable in order to use the Force Summation Method, which will be explained in Section 4.

$$P_k^{aero}(t) = q_\infty \cdot \left[A_0 w_j + A_1 \left(\frac{c_{ref}}{2V} \right) \dot{w}_j + A_2 \left(\frac{c_{ref}}{2V} \right)^2 \ddot{w}_j + A_3 \cdot lag_1 + A_4 \cdot lag_2 + \ldots + A_{n+2} \cdot lag_n \right] \tag{6}$$

A rational function approximation allows for a decomposition of the aerodynamic forces, given in Equation (6), into a steady term A_0 depending on the downwash w_j corresponding to Equation (3), a damping term A_1 depending on the change rate of the downwash $\dot{w}_j$ and a term A_2 depending on the acceleration of the downwash $\ddot{w}_j$. However, matrix A_2 is omitted during the approximation, as suggested by Kier and Looye [37]. The unsteady terms $A_3, A_4, \ldots, A_{n+2}$ depend on the lag states $lag_1, lag_{2,\ldots}, lag_n$. As the time simulation usually starts from an initial steady level flight, the lag states are assumed to be zero at the beginning. The lag state derivatives $\dot{lag}_i$ are given by Equation (7).

$$\dot{lag}_i = \dot{w}_j - \left(\frac{2V}{c_{ref}} \right) \cdot \beta_i \cdot w_j \tag{7}$$

$$\beta_i = \frac{k_{max}}{i} \tag{8}$$

In this work, the poles β_i used for the approximation are determined by Equation (8) given by Roger [35]. A slightly different proposal is given by ZONA [39]. Both methods were tested and showed comparable results. The quality of the approximation has to be checked carefully, because too few poles result in a bad approximation, leading to nonphysical results. For the Discus-2c, the selected number of poles is $n_{poles} = 6$ for the highest reduced frequency, $k_{max} = 1.0$.

The fuselage effect on the longitudinal aerodynamic properties is estimated as an additional pitching moment derivative due to the angle of attack $dCm/d\alpha$. The method from Truckenbrodt and Schlichting [40] is used for this approach. It consists of calculating the pitching moment characteristics of a slender body under influence of a straight wing within the limitations of potential aerodynamics. The fuselage contribution to the yawing moment due to sideslip $dCn/d\beta$ is estimated with handbook methods based on the slender-body theory [41]. The contribution of the fusealge is nevertheless small for both coefficients.

The aerodynamic forces and moments are calculated on the aerodynamic grid. The structural grid might be of much higher or lower discretization and in some cases, local coordinate systems might be used. This is one typical example where forces and moments need to be transferred from one grid to another. In addition, structural deflections need to be transferred back onto the aerodynamic grid. These operations can be handled with using the transformation matrix T_{di} which relates displacements of an independent grid u_i to displacements of a dependent grid u_d, as given in Equation (9). In addition, as in Equation (10), the transposed matrix T_{di}^T transforms forces and moments from a dependent grid P_d to an independent grid P_i.

$$u_d = T_{di} \cdot u_i \tag{9}$$

$$P_i = T_{di}^T \cdot P_d \tag{10}$$

The transformation matrix T_{di} may be defined by various methods. One commonly used approach for loads calculation is the rigid body spline. Each grid point of the dependent grid is mapped to exactly one point on the independent grid. The connection between these two grid points is assumed as a rigid body that transfers forces and moments. In addition, forces F create moments M due to their lever arm r as stated in Equation (11).

$$M = r \times F \tag{11}$$

In reverse, translations and rotations are directly transferred and rotations create additional translations. The mapping of the points may be defined manually or automatically, e.g. with a nearest neighbor search. As this concept is quite fast and versatile, it is selected for the aero-structural coupling in this work. The coupling model is shown in Figure 4. The small black lines between the blue and red dots visualize the mapping.

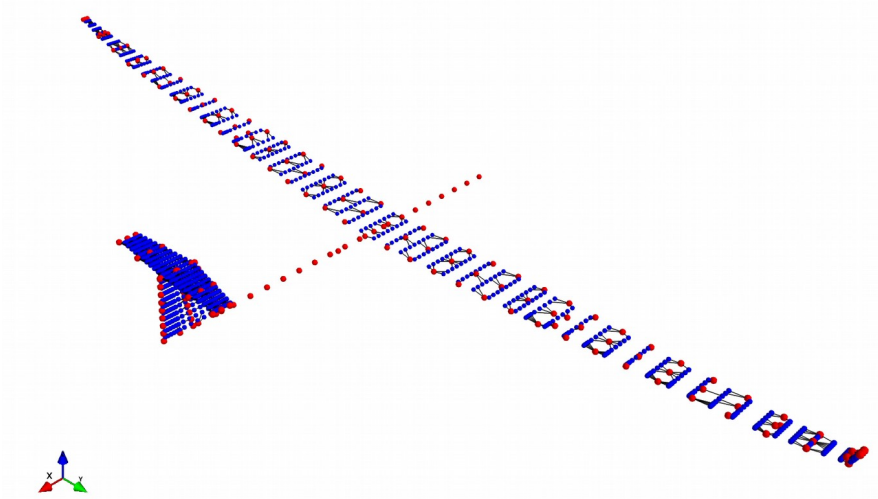

Figure 4: Coupling of the aerodynamic panel center points (blue) to the structural points (red) with a rigid body spline

4 EQUATION OF MOTION AND LOADS RECOVERY

The motion of the aircraft is divided into a rigid and a flexible part. For the rigid body motion, the aircraft is considered as a point mass with inertia matrices M_b and I_b, where the components of the inertia tensor I_b are calculated with respect to the body axes 'b'. Its origin is positioned at the center of gravity. All external forces and moments P_b^{ext} are gathered at the same point. The linear equations of motion, given in Equations (12) and (13), yield the translational and rotational accelerations $\dot{V}_b$ and $\dot{\Omega}_b$ of the aircraft body frame. Additional coupling terms between translation and rotation derived by Waszak, Schmidt and Buttrill [42–44] may be added at this point.

$$\dot{V}_b = M_b^{-1} \cdot P_b^{ext,\,forces} \tag{12}$$

$$\dot{\Omega}_b = I_b^{-1} \cdot P_b^{ext,\,moments} \tag{13}$$

In addition to the rigid body motion of the aircraft, linear structural dynamics are incorporated by Equation (14). Here, generalized external forces P_f^{ext} interact with linear elastic deflections u_f, velocities $\dot{u}_f$ and accelerations $\ddot{u}_f$. The matrices M_{ff}, D_{ff} and K_{ff} refer to the generalized mass, damping, and stiffness matrices. However, structural damping is assumed to be zero.

$$M_{ff}\ddot{u}_f + D_{ff}\dot{u}_f + K_{ff}u_f = P_f^{ext} \tag{14}$$

The resulting nodal loads P_g acting on the aircraft structure may be calculated by two different methods, the Mode Displacement Method [45] and the Force Summation Method [46]. The convergence of the Mode Displacement Method (MDM), given in Equation (15), strongly depends on the number of modes considered for the modal deformation vector u_f. The more modes are used, the more precise is the result. Using all modes, both methods should lead to identical results. With the Force Summation Method (FSM), given in Equation (16), the calculation is done using physical coordinates and the difference between inertia and external forces leads to the loads that are carried by the structure. In this work, the Force Summation Method is selected.

MDM:
$$P_g = K_g \cdot u_g = K_g \cdot \Phi_{fg} \cdot u_f \tag{15}$$

FSM:
$$P_g = P_g^{ext} - P_g^{iner} \tag{16}$$

From these nodal loads, so-called interesting quantities are calculated. Interesting quantities usually include cutting forces and moments at various stations (e.g. along the wing) and

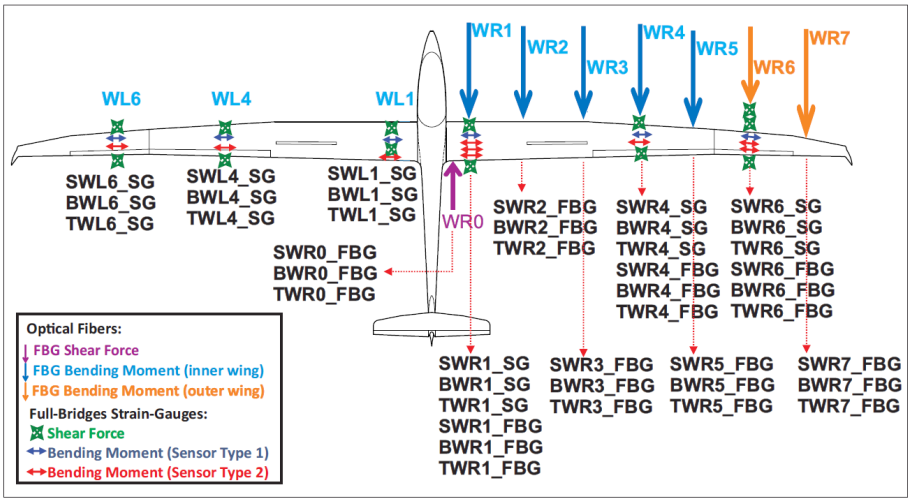

Figure 5: Measured internal forces and moments (shear, bending, torque) and positions

attachment loads (e.g. from control surfaces, payload, landing gear, etc.). These quantities are calculated at so-called monitoring stations. For the Discus-2c sailplane, monitoring stations along the wing (WR1, WR2, …) and the horizontal tail plane are defined in such a way that they are near the actual positions of the strain gauges. The positions of the mointoring stations are shown in Figure 5 whereas S, B and T stand for shear, bending and torque, BWR4_SG means for example Bending-Moment-Wing-Right-Position4-StrainGauge. The equations for calculating the internal forces and moments (shear, bending, torque) from the strain gauge measurements were developed by an extensive calibration program [15] and using the classical Skopinki method [47]. Additional optical strain sensors (Fiber-Bragg-Gratings, FBG) are installed inside the right wing but were not used.

In addition, structural grid points are placed at the locations of the accelerations sensors used during testing. They have no mass properties and are attached directly to the primary structure to be used as “numerical accelerometers”.

5 SOLUTION OF THE TRIM PROBLEM AND TIME DOMAIN SIMULATION

The calculation of aerodynamic forces and the evaluation of the equation of motion described in the previous Sections are cast into a single set of coupled equations. For the solution of this system, it is convenient to convert the equations into a first order system as shown in Equation (17).

$$\begin{pmatrix} \dot{u}_i \\ \ddot{u}_i \\ \dot{u}_f \\ \ddot{u}_f \\ \dot{u}_{cs} \end{pmatrix} = f \begin{pmatrix} u_i \\ \dot{u}_i \\ u_f \\ \dot{u}_f \\ u_{cs} \end{pmatrix} \tag{17}$$

In a next step, the trim conditions are defined. The vector u_i contains the aircraft position and Euler angles $(x, y, z, \Phi, \Theta, \Psi)^T$ with respect to the earth-fixed frame 'i', vector $\dot{u}_i$ the aircraft velocities and rates $(u, v, w, p, q, r)^T$, vector $\ddot{u}_i$ the aircraft translational and rotational accelerations $(\dot{u}, \dot{v}, \dot{w}, \dot{p}, \dot{q}, \dot{r})^T$ and vector u_{cs} the control commands about x, y and z axis $(\xi, \eta, \zeta)^T$. The trim conditions need to be set in such a way that they are not over- or under-determined in order to calculate one unique solution of the equations. The Discus-2c sailplane is assumed in a steady descending flight at a given velocity u before the maneuver starts. This requires the roll, pitch and yaw rates $\dot{p}, \dot{q}, \dot{r}$ to be zero while the control surface deflections ξ, η, ζ are flagged as free. In addition, $\dot{u}$ has to be zero so that the aircraft may not accelerate in horizontal direction. In exchange, a vertical velocity w is allowed. The equations are then solved with Powell's non-linear root-finding algorithm [48–50]. Once this initial flight condition is found, a time simulation is started.

The time simulation is performed by an integration of Equation (17) over a period of time. Two different integration schemes have been tested. The explicit runge-kutta method of 4th/5th order [51] and an implicit Adams-Bashforth method [52], both implemented in scipy [53], have shown numerically equivalent results. Because of the fewer function evaluations, the Adams-Bashforth method was selected. During the integration, the rate of change of the control surface deflections $\dot{u}_{cs}$ is fed into the simulation. The rate of change is calculated numerically from the control surface deflections u_{cs} recorded during flight test using a backward differences quotient of first order.

One key element of the simulation is the feedback of the aircraft speed. In Figure 6, the loss of altitude during a vertical maneuver is shown. Within four seconds of time, the aircraft looses about 20 meters of altitude. Such a sink rate is very high for a normal sailplane and

results in a gain of true airspeed V_{tas} of about three meters per second. Assuming constant air density, the dynamic pressure $q_\infty = \rho/2 \cdot V_{tas}^2$ is increased by ~18%, causing more lift so that the sailplane would return automatically into a normal, horizontal flight condition. Most commercial software packages assume a constant dynamic pressure, which would lead to an unphysical, diverging behavior of the aircraft.

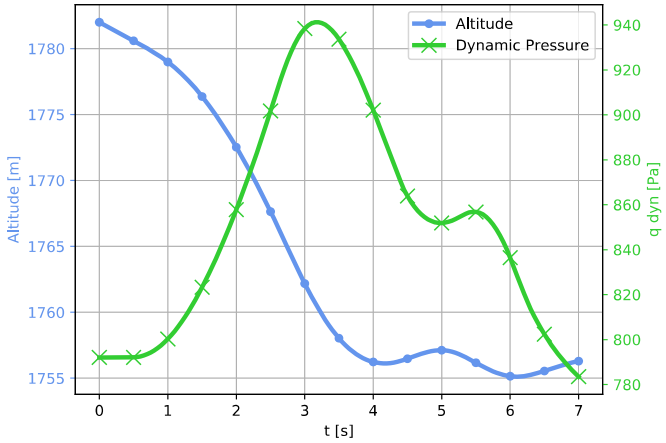

Figure 6: Loss of altitude and gain of dynamic pressure during a vertical maneuver

6 FLIGHT TEST AND LOADS MEASUREMENTS OF THE DISCUS-2C

The DLR Discus-2c is equipped with a complex flight test instrumentation which provides the possibility of measuring loads and accelerations at different parts of the aircraft structure. Therefore, strain gauges, Fiber-Bragg-Gratings and 3-axis accelerometers were already installed inside the aircraft structure during manufacturing. The main flight test data acquisition system is installed in the engine compartment where also a high precision inertial measurement unit (IMU) is located. Angles of attack and sideslip are measured by a 5-hole probe installed on a nose boom. For recording the control surface deflections, potentiometers are used. Figure 7 gives an overview of all installed sensors. The strain gauges are interconnected as full bridges so that thermal strains are canceled out. Overall, 46 strain gauge full bridges and 14 3-axis accelerometers are placed in wing, horizontal tail and fuselage. All measurements are recorded with a sample rate of 100 Hz. As mentioned in Section 4, an extensive experimental test program was conducted to calibrate the sensor signals obtaining the internal loads at certain positions [16,47,54]. In addition to the strain and acceleration sensors, the following measurements were recorded during flight test:

- static and dynamic pressure
- indicated and true airspeed (IAS, TAS)
- barometric altitude
- vertical speed based on barometric altitude
- static temperature
- angle of attack α and sideslip β (uncalibrated)
- ground and vertical speed
- GPS position
- accelerations $Acc_{x,y,z}$ and rotational speeds p, q, r (IMU)
- euler angles Φ, Θ, Ψ (IMU)
- control surface deflections of ailerons ξ, elevator η, rudder ζ and airbrakes

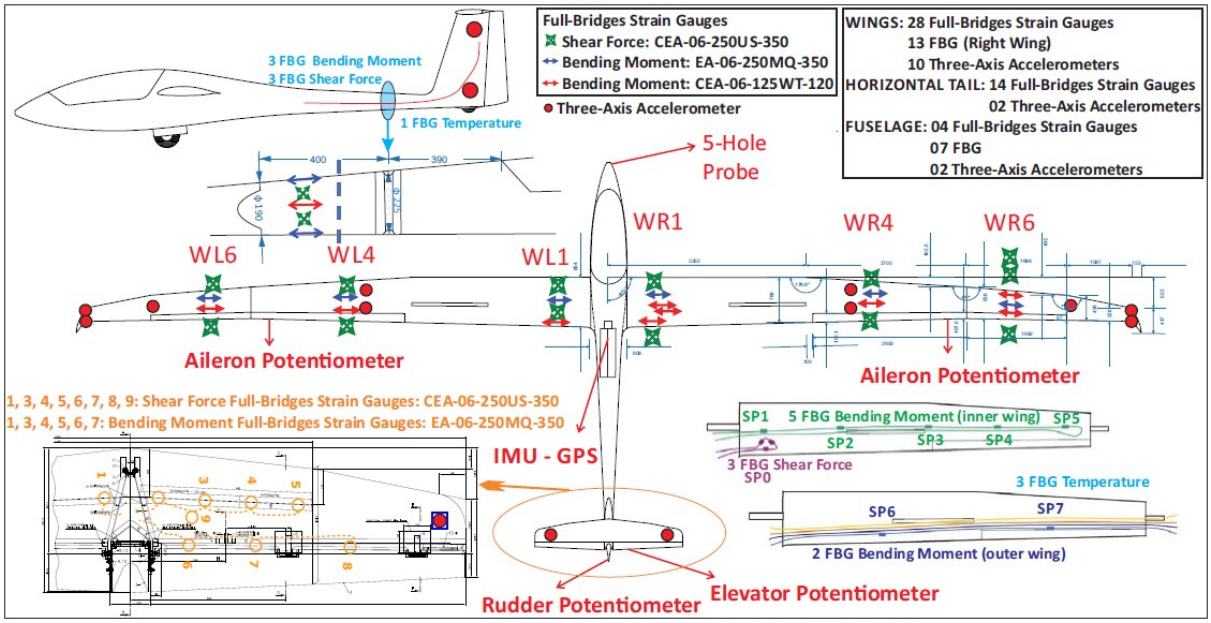

Figure 7: Overview of DLR Discus-2c flight test instrumentation

During the flight test campaign, an overall of 22 flights including 396 maneuvers in longitudinal and lateral motion were conducted at different test points (altitude and speed). Figure 8 shows typical control surface inputs for excitation of rigid body and flexible modes. The sailplane was towed up to an altitude of 3000m. Selected test points were placed during descent at different speeds of 100, 130 and 160 km/h. For checking the recorded data quality directly after flight, a special software was developed which allows for an evaluation of the pilot inputs as well as finding inconsistencies in the data recording (sensor failures, dropouts, etc.).

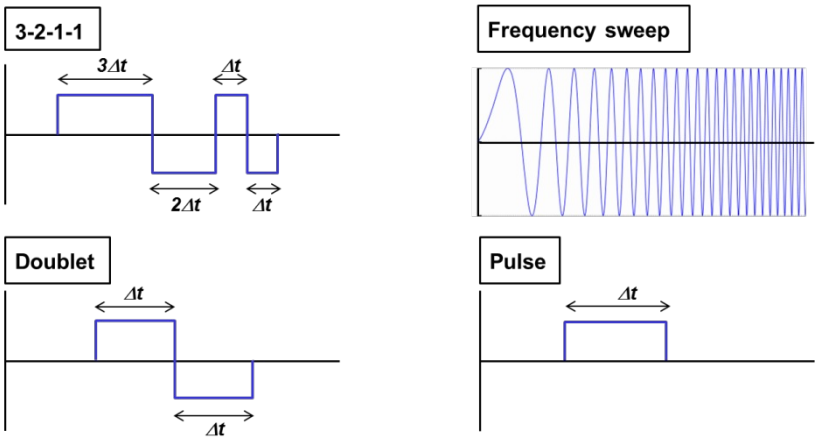

Figure 8: Typical control surface inputs for system identification and loads analysis

7 COMPARISON OF RESULTS

In the following, the rigid body motion, section forces and structural accelerations from the numerical simulation are compared to the data obtained during flight test. Two vertical maneuvers with a 3-2-1-1 elevator input and two rolling maneuvers with aileron input are calculated. The rolling maneuvers turned out to be more difficult. One reason for this is that loads due to vertical maneuvers are high while the aircraft motion is small. This is different for the rolling maneuvers, where for example the bank angle is very high while the loads are lower. In addition, the aircraft motion is not pure rolling but an interaction with lateral and

vertical motion. In general, large motions are difficult to capture precisely as the tools used for loads simulations were not designed with a flight mechanical focus in mind. In the following, exemplary results for both the vertical and the rolling maneuvers are shown and discussed.

7.1 Vertical Maneuvers

The rigid body motion during the vertical maneuvers are compared using the aircraft acceleration in z direction, the euler angle θ and the pitch rate q. They are shown in Figures 9, 10 and 11. The agreement is very good, even towards the end of the simulation time. For this kind of flight maneuver, the pilot's elevator input η is the primary control command. In addition, the aileron input ξ is included in the simulation, because it might cause additional aerodynamic forces. The drawback is clearly visible when looking at the role rate p in Figure 11. During the flight, the sailplane is subject to atmospheric turbulence and the sailplane experiences a slight rolling motion, which the pilot tries to compensate, e.g. between 3.5 and 4.5 seconds or between 5.0 and 6.5 seconds.

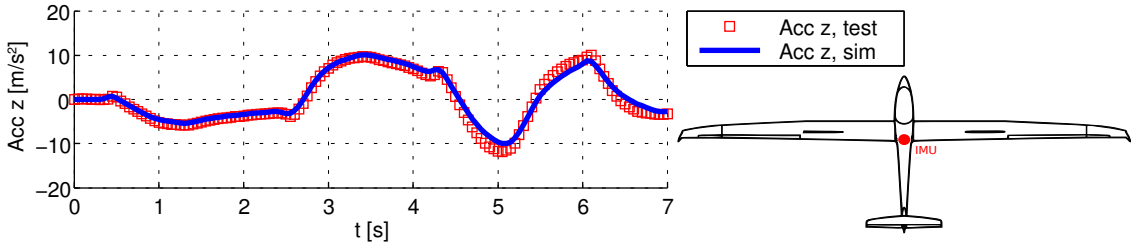

Figure 9: Comparison of rigid body acceleration in z-direction

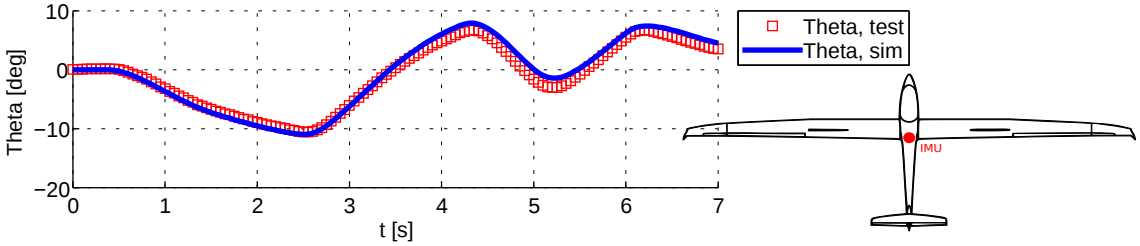

Figure 10: Comparison of pitch angle θ

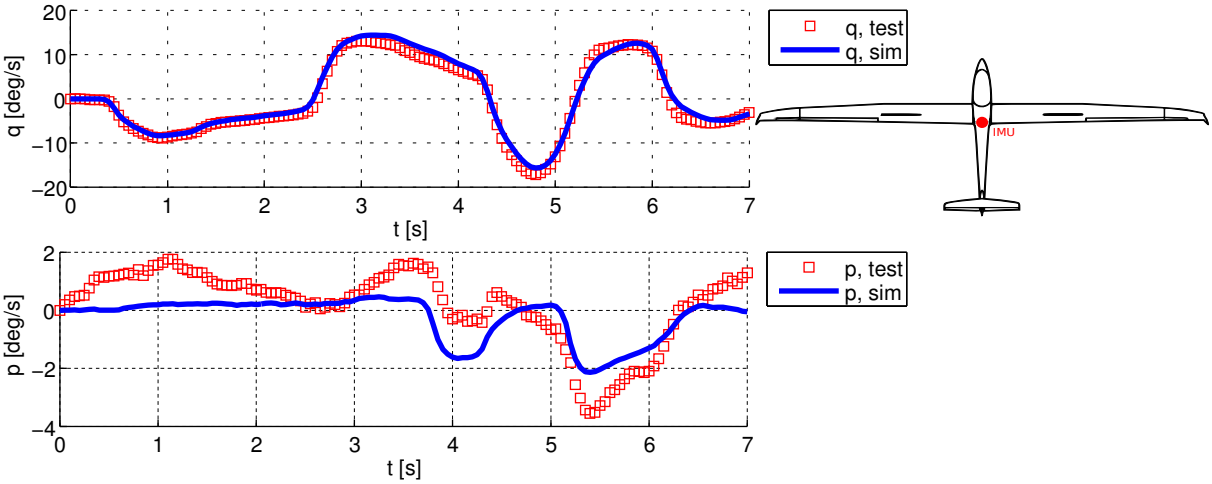

Figure 11: Comparison of pitch rate q and roll rate p

In Figure 12, the section loads at the right wing root are shown. Both the shear forces F_z and the bending moments M_x show a very good agreement with a slight underestimation

compared to the measurements around 5.0 seconds. The outer wing shear forces F_z and the bending moments M_x shown in Figure 13 have a similar shape with a lower amplitude.

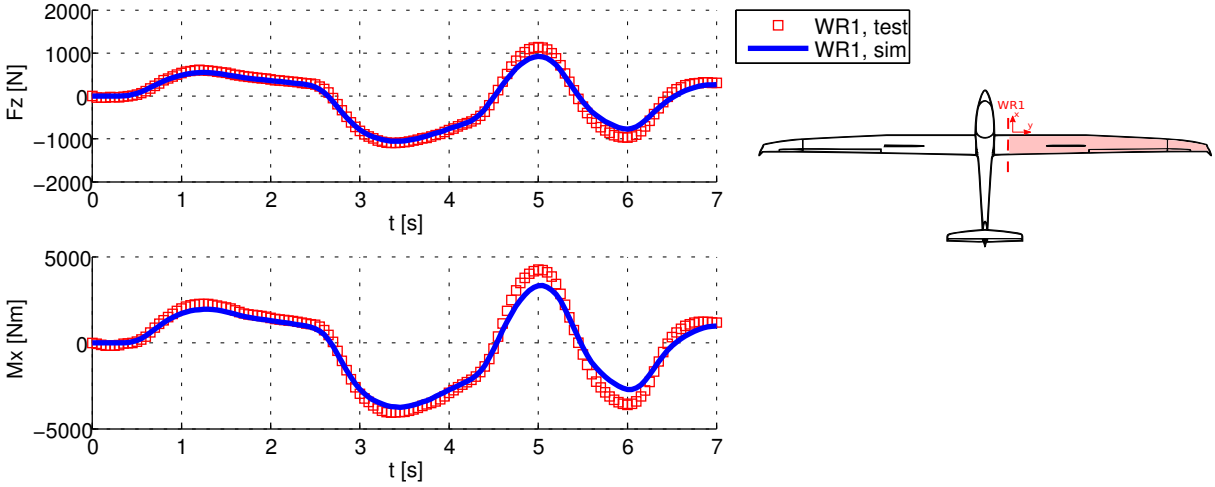

Figure 12: Comparison of right wing root shear force F_z and bending moment M_x

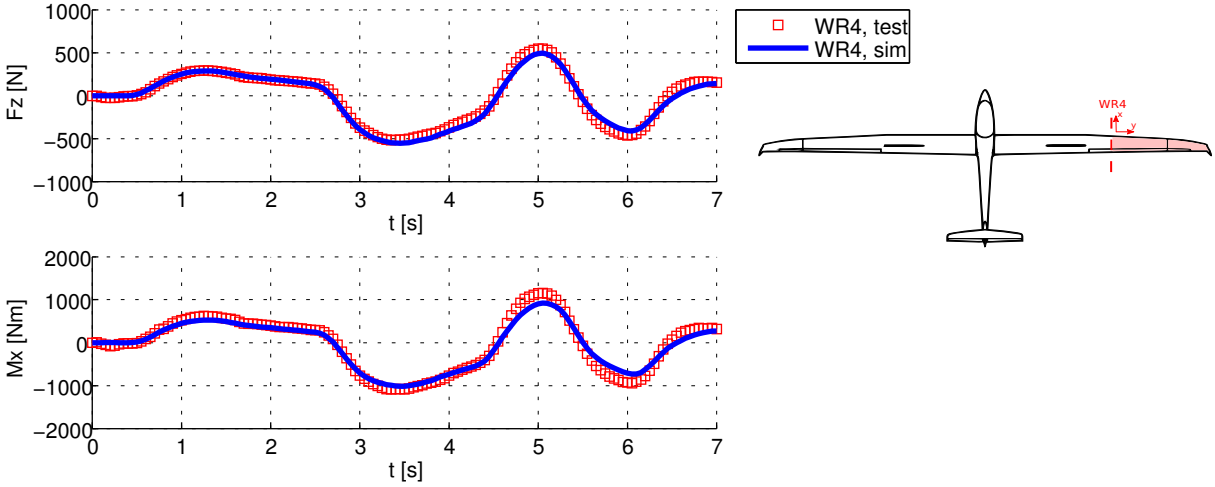

Figure 13: Comparison of right outer wing shear force F_z and bending moment M_x

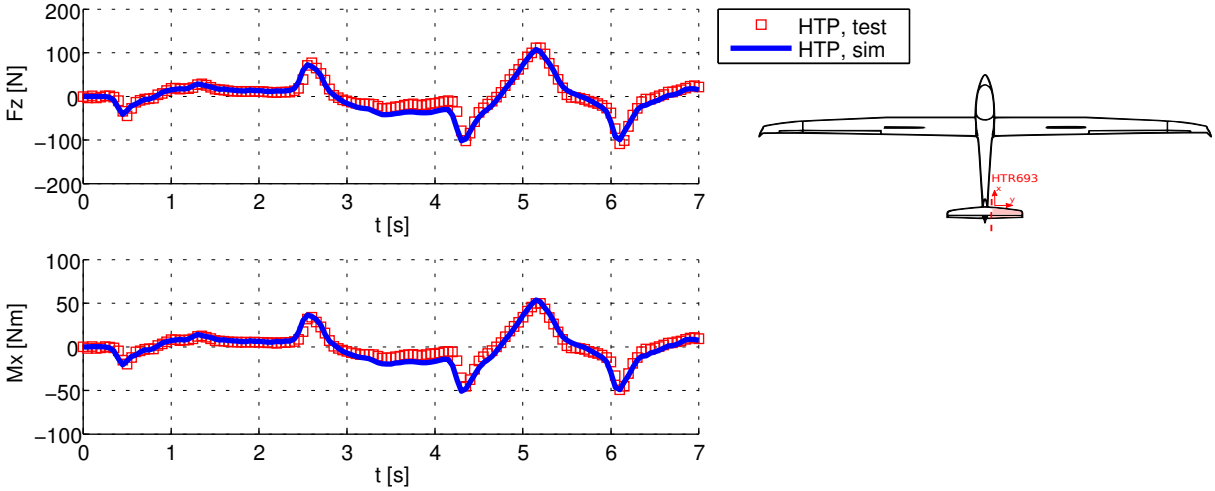

Figure 14: Comparison of horizontal tail plane shear force F_z and bending moment M_x

Looking at the shear forces F_z and the bending moments M_x at the horizontal tail plane shown in Figure 14, one can see several pronounced peaks each time the pilot changes the elevator deflection. Once the aircraft starts to pitch (compare pitch rate in Figure 11), the loads on the horizontal tail are reduced. Figure 15 shows the acceleration in z-direction of the right wing tip. Although the measurement data is scattered, there is a very good agreement

with the simulation. Even small, minor peaks occurring e.g. around 2.8, 4.5, 5.5 and 6.3 seconds are captured well.

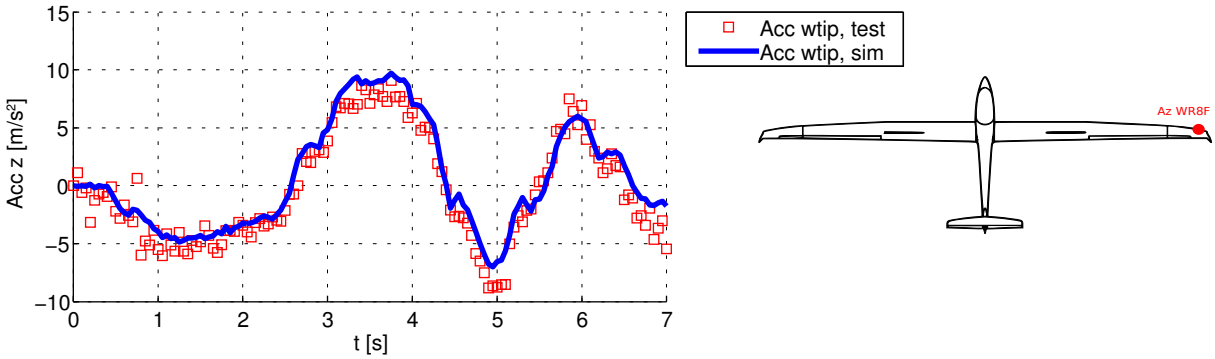

Figure 15: Comparison of right wing tip acceleration in z-direction

Another objective of this study is to asses the need of structural dynamics and unsteady aerodynamics. As an example, the right wing root shear force F_z is analyzed in more detail. In Figure 16 on the left, the shear force due to aerodynamic force is plotted with green squares while the inertia force is plotted with cyan crosses. The sum of both leads to the total force, plotted with blue dots. This line corresponds to the blue line shown previously in Figure 12. With red triangles the unsteady aerodynamic force and with black stars the aerodynamic force due to structural flexibility are plotted. One can see that both are small compared to the total force with blue dots. In Figure 16 on the right, the individual forces are scaled by the total force. In this way one can see that both the unsteady aerodynamic force and the aerodynamic force due to structural flexibility have a contribution of approximately 10% to the total force with a peak of approximately 15% at 5.0 seconds.

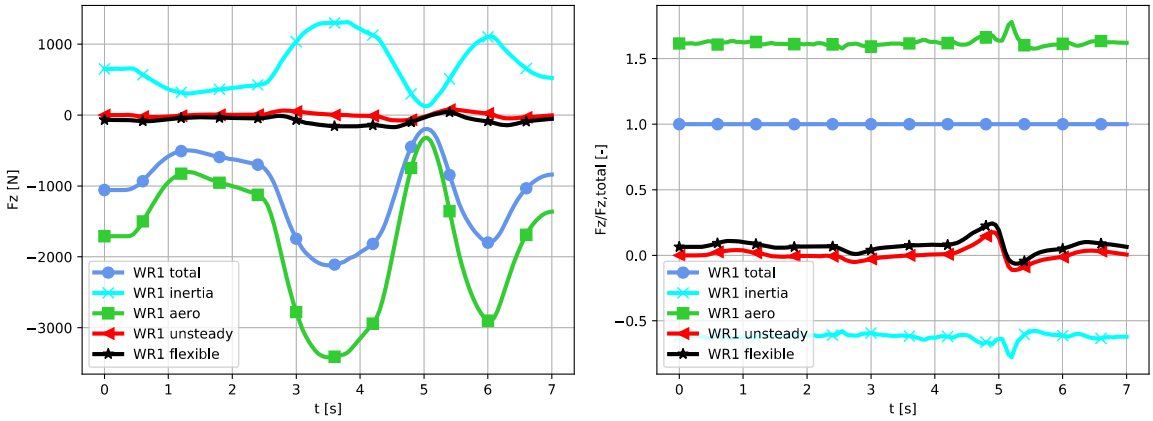

Figure 16: Force contributions to the right wing root shear forces F_z in detail

7.2 Rolling Maneuvers

The rigid body motion of the rolling maneuvers are compared using the acceleration in y and z direction, the bank angle φ and the roll rate p. These data are shown in Figures 17, 18 and 19 respectively. The agreement of the results is not as good as for the vertical maneuvers, but still acceptable. In addition to the lateral motion, there is also a vertical component. Therefore, in Figure 19 the pitch and yaw rates q and r are shown as well. Looking only at the green, dotted curves, the disagreement is stronger. The reason for this deviation can be explained by the fuselage, which is missing in the aerodynamic model. A closer investigation yields that the simulation model is much more stable in lateral direction than the real sailplane. This is because the fuselage has a destabilizing effect. As described in Section 3, coefficients for the pitching moment due to the angle of attack $dCm/d\alpha$ and the yawing

moment due to sideslip $dCn/d\beta$ have been added to compensate this shortcoming. The results with these coefficients are plotted as continuous, blue curves. The coefficients show a significant impact on the acceleration in z-direction and on the pitch and yaw rates q and r. The results now deviate much less from flight test.

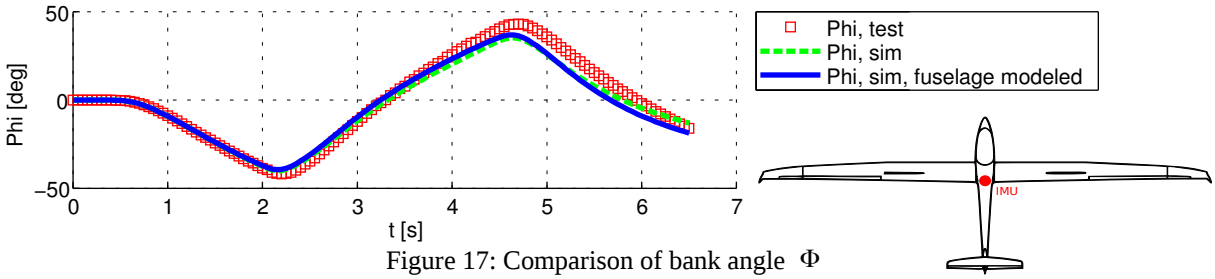

Figure 17: Comparison of bank angle Φ

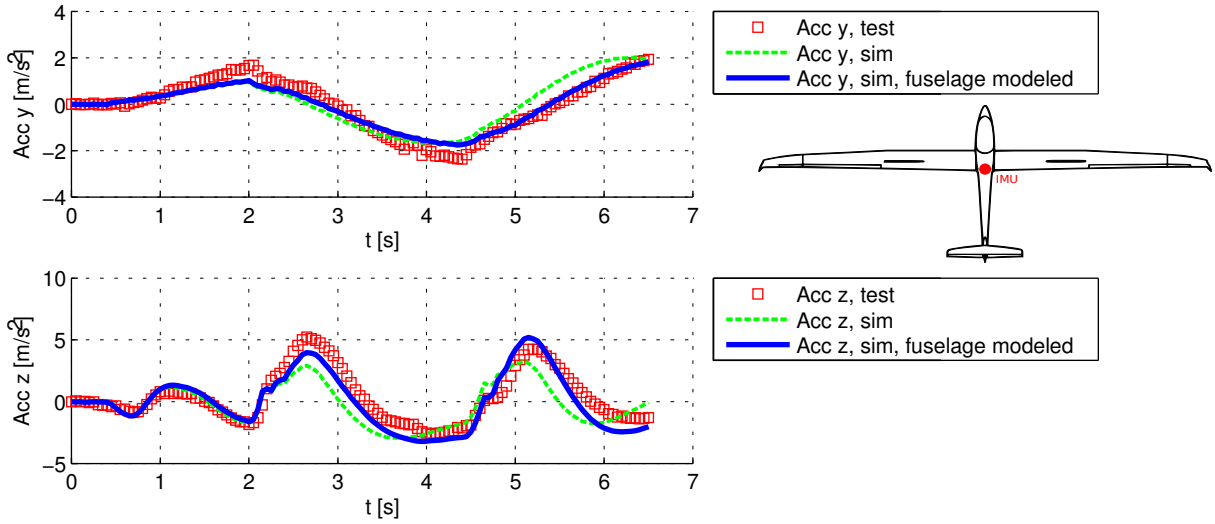

Figure 18: Comparison of rigid body accelerations in y and z-direction

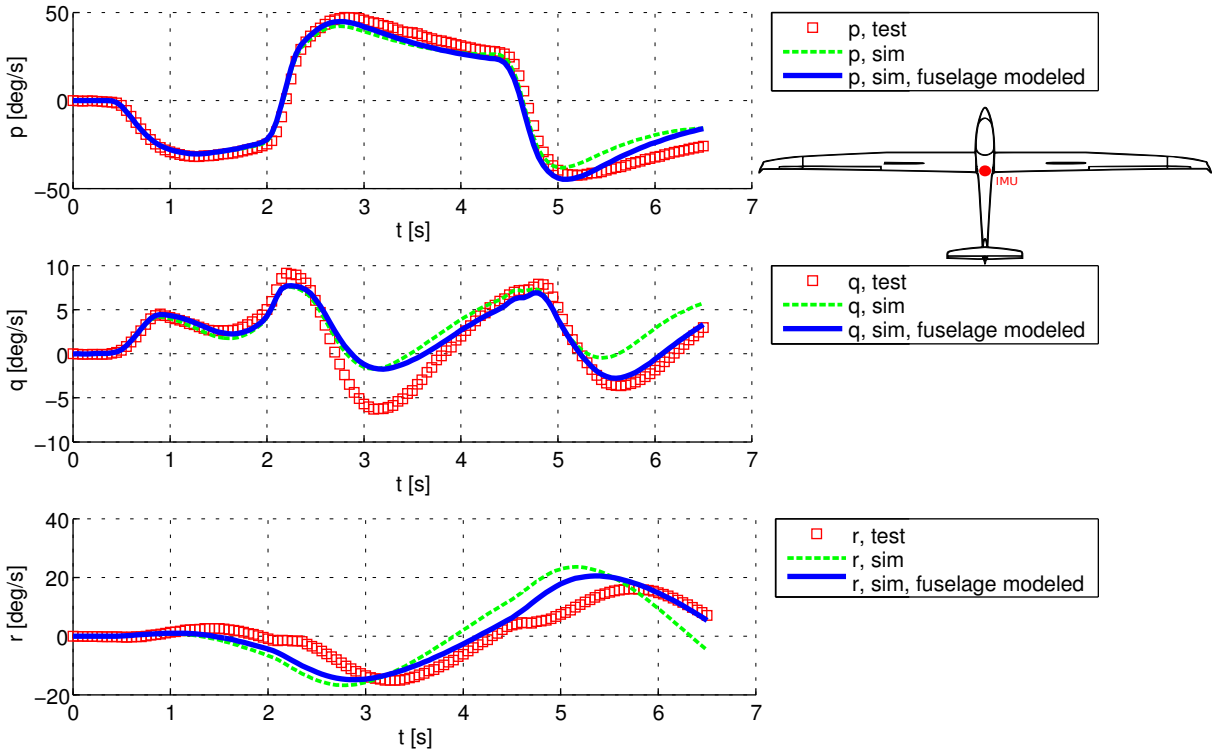

Figure 19: Comparison of roll, pitch and yaw rates p, q, r

Looking at the section loads at the right wing root in Figure 20, both the shear forces F_z and the bending moments M_x show a very good agreement with the flight test. One can see a slight deviation between 2.5 and 4.5 seconds. This deviation is also visible in the pitch rate q in Figure 19. This would lead to a temporarily higher angle of attack at the wing, causing higher loads.

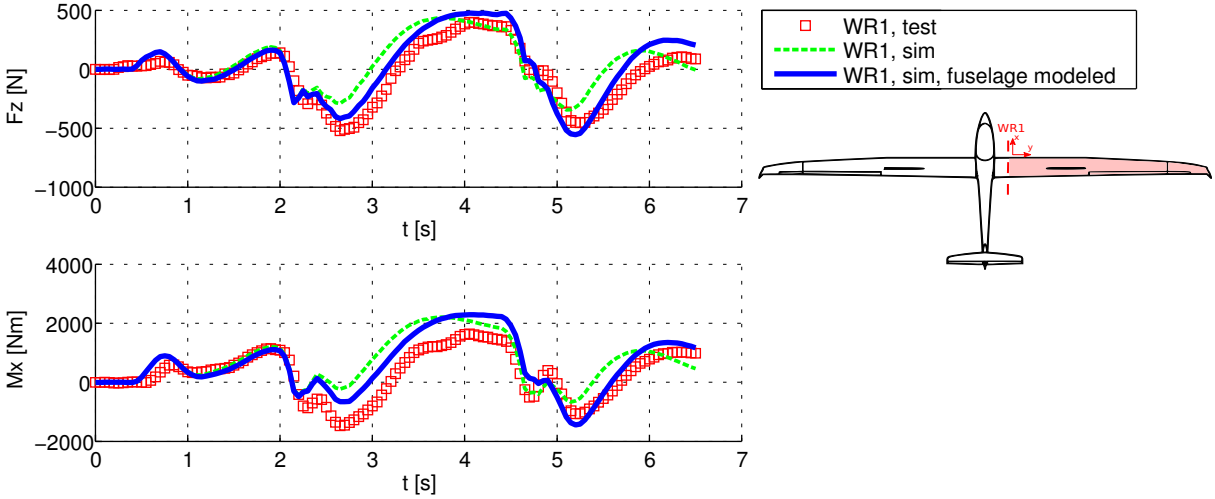

Figure 20: Comparison of right wing root shear forces F_z and bending moments M_x

8 CONCLUSION AND OUTLOOK

In this work, a comparison of dynamic maneuver loads for the Discus-c2 sailplane obtained from simulation and flight test is presented. The stiffness and mass models are set-up using simplified formulations derived from the preliminary design for the replication of an existing sailplane. The selected methods and resulting mass, stiffness, aerodynamic models have proven to be appropriate for dynamic maneuver loads analyses. In a next step, the loads process was tested with two vertical maneuvers with elevator deflections and two rolling maneuvers with aileron deflections. The resulting rigid body motion, section forces and structural accelerations have been compared to the data obtained from flight test. The dynamic increments of the vertical maneuvers show a very good agreement while the rolling maneuvers turned out to be more difficult. The results were improved by adding coefficients for the pitching moment due to the angle of attack $dCm/d\alpha$ and the yawing moment due to sideslip $dCn/d\beta$ to account for the influence of the fuselage. In general, the results exceeded expectations and the simulation was validated against flight test successfully.

In the future, the induced drag will be considered in the simulation. This might improve the rolling simulations further. Also, for the torsional moment M_y, the simulation sometimes did not match the measurement data. This was the case e.g. at the wing root. One presumption is that the measurement of M_y is difficult because the monitoring station is in close proximity the the fuselage, which might have an influence. In addition, M_y is usually very sensitive and small modifications in the structural or mass model might have a large impact. A better knowledge of the actual structure and mass distributions in chord wise direction would help to improve the models.

Furthermore, additional flight maneuvers might be analyzed. Among others, there are rolling maneuvers with faster and shorter aileron deflections and maneuvers with increasing frequency. They might be interesting because the lateral motion is smaller and unsteady aerodynamics might become more important.

REFERENCES

[1] Handojo, V., and Klimmek, T., “Böenlastanalyse der vorwärts gepfeilten ALLEGRA-Konfiguration,” presented at the Deutscher Luft- und Raumfahrtkongress, Rostock, 2015.

[2] Klimmek, T., “Parametric Set-Up of a Structural Model for FERMAT Configuration for Aeroelastic and Loads Analysis,” *Journal of Aeroelasticity and Structural Dynamics*, no. 2, pp. 31–49, May 2014.

[3] Krüger, W. R., Klimmek, T., Liepelt, R., Schmidt, H., Waitz, S., and Cumnuantip, S., “Design and aeroelastic assessment of a forward-swept wing aircraft,” *CEAS Aeronautical Journal*, vol. 5, no. 4, pp. 419–433, 2014.

[4] Liersch, C. M., and Huber, K. C., “Conceptual Design and Aerodynamic Analyses of a Generic UCAV Configuration,” presented at the 32nd AIAA Applied Aerodynamics Conference, Atlanta, GA, 2014.

[5] Pinho Chiozzotto, G., “Conceptual design method for the wing weight estimation of strut-braced wing aircraft,” presented at the 5th CEAS Air & Space Conference, Delft, The Netherlands, 2015.

[6] Voß, A., and Klimmek, T., “Design and sizing of a parametric structural model for a UCAV configuration for loads and aeroelastic analysis,” *CEAS Aeronaut J*, vol. 8, no. 1, pp. 67–77, Mar. 2017.

[7] Voß, A., and Klimmek, T., “Maneuver Loads Calculation with Enhanced Aerodynamics for a UCAV Configuration,” presented at the AIAA Modeling and Simulation Technologies Conference, Washington, D.C., 2016.

[8] Krüger, W., Handojo, V., and Klimmek, T., “Flight Loads Analysis and Measurements of External Stores on an Atmospheric Research Aircraft,” presented at the 58th AIAA/ASCE/AHS/ASC Structures, Structural Dynamics, and Materials Conference, Grapevine, Texas, 2017.

[9] “DLR’s research aircraft,” *Research Aircraft*. [Online]. Available: http://www.dlr.de/dlr/en/desktopdefault.aspx/tabid-10203/. [Accessed: 21-Apr-2017].

[10] Krüger, W., and Klimmek, T., “Definition of a Comprehensive Loads Process in the DLR Project iLOADS,” presented at the Deutscher Luft- und Raumfahrtkongress, Braunschweig, Deutschland, 2016.

[11] Klimmek, T., Ohme, P., Ciampa, and Handojo, V., “Aircraft Loads – An Important Task from Pre-Design to Loads Flight Testing,” presented at the Deutscher Luft- und Raumfahrtkongress, Braunschweig, 2016.

[12] Cumnuantip, S., Kier, T., and Pinho Chiozzotto, G., “Methods for the Quantification of Aircraft Loads in DLR-Project iLOADS,” presented at the Deutscher Luft- und Raumfahrtkongress, 2016.

[13] Sinske, J., Govers, Y., Handojo, V., and Krüger, W. R., “HALO Flugtest mit instrumentierten Aussenlasten fuer Aeroelastik- und Lastmessungen im DLR Projekt iLOADS,” presented at the Deutscher Luft- und Raumfahrtkongress, Braunschweig, 2016.

[14] “Discus-2c DLR,” *Research Aircraft*. [Online]. Available: http://www.dlr.de/dlr/en/desktopdefault.aspx/tabid-10203/339_read-9181/#/gallery/8791. [Accessed: 03-Apr-2017].

[15] Preisighe Viana, M. V., “Sensor calibration for calculation of loads on a flexible aircraft,” presented at the 16th International Forum on Aeroelasticity and Structural Dynamics, Saint Petersburg, Russia, 2015.

[16] Ohme, P., Raab, C., and Preisighe Viana, M. V., “Lastenmessung im Flugversuch und Entwicklung Echtzeitfähiger Simulationsmodelle,” presented at the Deutscher Kongress für Luft- und Raumfahrt, Braunschweig, 2016.

[17] Preisighe Viana, M. V., “Time-Domain System Identification of Rigid-Body Multipoint Loads Model,” presented at the AIAA Atmospheric Flight Mechanics Conference, Washington, D.C., 2016.
[18] Montel, M., and Thielecke, F., “Validation of a nonlinear observer implementation for empennage loads estimation,” *CEAS Aeronautical Journal*, vol. 7, no. 2, pp. 299–313, Jun. 2016.
[19] Eller, D., “On an efficient method for time-domain computational aeroelasticity,” Dissertation, KTH Royal Institute of Technology, Stockholm, 2005.
[20] Eller, D., and Ringertz, U., “Aeroelastic Simulations of a Sailplane,” Department of Aeronautical and Vehicle Engineering, KTH, 2005.
[21] Ramsey, H. D., and Lewolt, J. G., “Design maneuver loads for an airplane with an active control system,” presented at the 20th Structures, Structural Dynamics, and Materials Conference, St. Louis, USA, 1979.
[22] Stauffer, W. A., and Hoblit, F. M., “Dynamic gust, landing, and taxi loads determination in the design ofthe L-1011.,” *Journal of Aircraft*, vol. 10, no. 8, pp. 459–467, 1973.
[23] Stauffer, W. A., Lewolt, J. G., and Hoblit, F. M., “Application of Advanced Methods to Design Loads Determination for the L-1011 Transport,” *Journal of Aircraft*, vol. 10, no. 8, pp. 449–458, 1973.
[24] Climent, H., Lindenau, O., Claverias, S., Viana, J. T., Oliver, M., Benitez, L., Pfeifer, D., and Jenaro-Rabadan, G., “Flight Test Validation of Wake Vortex Encounter Loads,” presented at the International Forum for Aeroelasticity and Structural Dynamics, Bristol, United Kingdom, 2013.
[25] Claverias, S., Cerezo, J., Torralba, M. A., Reyes, M., Climent, H., and Karpel, M., “Wake Vortex Encounter Loads Numerical Simulation,” presented at the International Forum for Aeroelasticity and Structural Dynamics, Bristol, United Kingdom, 2013.
[26] Schrenk, O., “Ein einfaches Näherungsverfahren zur Ermittlung von Auftriebsverteilungen längs der Tragflügelspannweite,” Aerodynamische Versuchsanstalt (AVA), Göttingen, Germany, 1940.
[27] Katz, J., and Plotkin, A., *Low-speed aerodynamics: from wing theory to panel methods*. New York: McGraw-Hill, 1991.
[28] Albano, E., and Rodden, W. P., “A Doublet Lattice Method For Calculating Lift Distributions on Oscillation Surfaces in Subsonic Flows,” in *AIAA 6th Aerospace Sciences Meeting*, New York, 1968.
[29] Blair, M., “A Compilation of the Mathematics Leading to The Doublet Lattice Method,” Airforce Wright Laboratory, Ohio, Technical Report WL-TR-92-3028, 1992.
[30] Kotikalpudi, A., “Body Freedom Flutter (BFF) Doublet Lattice Method (DLM),” *University of Minnesota Digital Conservancy*, 09-Sep-2014. [Online]. Available: http://hdl.handle.net/11299/165566. [Accessed: 12-Feb-2016].
[31] Kotikalpudi, A., Pfifer, H., and Balas, G. J., “Unsteady Aerodynamics Modeling for a Flexible Unmanned Air Vehicle,” presented at the AIAA Atmospheric Flight Mechanics Conference, Dallas, Texas, 2015.
[32] Hedman, S. G., “Vortex Lattice Method for Calculation of Quasi Steady State Loadings on Thin Elastic Wings in Subsonic Flow,” FFA Flygtekniska Försöksanstalten, Stockholm, Sweden, FFA Report 105, 1966.
[33] Rodden, W. P., Giesing, J. P., and Kálmán, T. P., “New Developments and Application of the Subsonic Doublet-Lattice Method for Nonplanar Configurations,” *AGARD-CP-80-PT-2 - Symposium on Unsteady Aerodynamics for Aeroelastic Analyses of Interfering Surfaces*, no. Part 2, Jan. 1971.
[34] Rodden, W., MacNeal, Harder, R., McLean, and Bellinger, D., *MSC.Nastran Version 68 Aeroelastic Analysis User’s Guide*. MSC.Software Corporation, 2010.
[35] Roger, K. L., “Airplane Math Modeling Methods For Active Control Design,” in

AGARD-CP-228, 1977.
[36] Gupta, K. K., Brenner, M. J., and Voelker, L. S., “Developement of an Integrated Aeroservoelastic Analysis Program and Correlation With Test Data,” Dryden Flight Research Facility, Edwards, California, Technical Paper NASA Technical Paper 3120, 1991.
[37] Kier, T., and Looye, G., “Unifying Manoeuver and Gust Loads Analysis Models,” presented at the International Forum for Aeroelasticity and Structural Dynamics, 2009.
[38] Karpel, M., and Strul, E., “Minimum-state unsteady aerodynamic approximations with flexible constraints,” *Journal of Aircraft*, vol. 33, no. 6, pp. 1190–1196, Nov. 1996.
[39] ZONA Technology Inc., *ZAERO Theoretical Manual*, vol. Version 9.0. Scottsdale, Arizona, 2014.
[40] Schlichting, H., and Truckenbrodt, E., *Aerodynamik des Flugzeuges: Aerodynamik des Tragflügels (Teil 2), des Rumpfes, der Flügel-Rumpf-Anordnung und Leitwerke*, Zweite neubearbeitete Auflage. Springer-Verlag, 1969.
[41] Nicolai, L. M., and Carichner, G. E., *Fundamentals of Aircraft and Airship Design: Volume I Aircraft Design*. Reston, VA: American Institute of Aeronautics and Astronautics, 2010.
[42] Waszak, M. R., and Schmidt, D. K., “Flight dynamics of aeroelastic vehicles,” *Journal of Aircraft*, vol. 25, no. 6, pp. 563–571, Jun. 1988.
[43] Buttrill, C., Arbuckle, P., and Zeiler, T., “Nonlinear simulation of a flexible aircraft in maneuvering flight,” presented at the Flight Simulation Technologies Conference, Guidance, Navigation, and Control and Co-located Conferences, 1987.
[44] Waszak, M., Buttrill, C., and Schmidt, D., “Modeling and Model Simplification of Aeroelastic Vehicles: An Overview,” NASA Langley Research Center, NASA Technical Memorandum 107691, Sep. 1992.
[45] Bisplinghoff, R. L., and Ashley, H., *Principles of Aeroelasticity*. Dover Publications, 2002.
[46] Reschke, “Integrated Flight Loads Modelling and Analysis for Flexible Transport Aircraft,” Dissertation, Universität Stuttgart, Oberpfaffenhofen, Germany, 2006.
[47] Skopinski, T. H., Aiken, W. S., and Huston, W. B., “Calibration of strain-gage installations in aircraft structures for the measurement of flight loads,” National Advisory Committee for Aeronautics. Langley Aeronautical Lab, Langley Field, VA, Technical Report NACA-TR-1178, Jan. 1954.
[48] Garbow, B. S., Hillstrom, K. E., and More, J. J., “minpack/hybrd.html,” *Documentation for MINPACK subroutine HYBRD*, 1980. [Online]. Available: https://www.math.utah.edu/software/minpack/minpack/hybrd.html. [Accessed: 20-Apr-2017].
[49] Powell, M. J., “A hybrid method for nonlinear equations,” *Numerical methods for nonlinear algebraic equations*, vol. 7, pp. 87–114, 1970.
[50] The Scipy community, “scipy.optimize.fsolve,” *SciPy v0.17.0 Reference Guide*. [Online]. Available: http://docs.scipy.org/doc/scipy/reference/generated/scipy.optimize.fsolve.html. [Accessed: 24-Feb-2016].
[51] Dormand, J. R., and Prince, P. J., “A family of embedded Runge-Kutta formulae,” *Journal of Computational and Applied Mathematics*, vol. 6, no. 1, pp. 19–26, Mar. 1980.
[52] Brown, P. N., Byrne, G. D., and Hindmarsh, A. C., “VODE: A Variable-Coefficient ODE Solver,” *SIAM Journal on Scientific and Statistical Computing*, vol. 10, no. 5, pp. 1038–1051, Sep. 1989.
[53] “scipy.integrate.ode,” *SciPy v0.18.0 Reference Guide*. [Online]. Available: http://docs.scipy.org/doc/scipy/reference/generated/scipy.integrate.ode.html#scipy.integrate.ode. [Accessed: 08-Aug-2016].
[54] Preisighe Viana, M. V., “Multipoint Model for Flexible Aircraft Loads Monitoring in Real Time,” Dissertation, TU Braunschweig, Braunschweig, Deutschland, 2016.

COPYRIGHT STATEMENT